Live-pig-airway surface imaging and whole-pig CT at the Australian Synchrotron Imaging and Medical Beamline

Martin Donnelley,[a,b,c*] Kaye S. Morgan,[d,e,f] Regine Gradl,[e,f] Mitzi Klein,[g] Daniel Hausermann,[g] Chris Hall,[g] Anton Maksimenko[g] and David W. Parsons[a,b,c]

[a]Robinson Research Institute, University of Adelaide, SA 5001, Australia, [b]Respiratory and Sleep Medicine, Women's and Children's Hospital, 72 King William Road, North Adelaide, SA 5006, Australia, [c]Adelaide Medical School, University of Adelaide, SA 5001, Australia, [d]School of Physics, Monash University, Clayton, Vic 3800, Australia, [e]Institute for Advanced Study, Technische Universität München, 85748 Garching, Germany, [f]Chair of Biomedical Physics and Munich School of BioEngineering, Technische Universität München, 85748 Garching, Germany, and [g]Imaging and Medical Beamline, Australian Synchrotron, Clayton, Vic 3800, Australia.
*Correspondence e-mail: martin.donnelley@adelaide.edu.au

The Australian Synchrotron Imaging and Medical Beamline (IMBL) was designed to be the world's widest synchrotron X-ray beam, partly to enable clinical imaging and therapeutic applications for humans, as well as for imaging large-animal models. Our group is currently interested in imaging the airways of newly developed cystic fibrosis (CF) animal models that display human-like lung disease, such as the CF pig. One key outcome measure for assessing the effectiveness of CF airway therapies is the ability of the lung to clear inhaled particulates by mucociliary transit (MCT). This study extends the *ex vivo* sheep and pig tracheal-tissue studies previously performed by the authors at the IMBL. In the present study, attempts were made to determine whether the design of the IMBL is suitable for imaging tracheal MCT in live pigs. The movement of 200 µm-diameter high-refractive-index (HRI) glass-bead marker particles deposited onto the tracheal airway surface of eight live piglets was tracked and quantified and the MCT response to aerosol delivery was examined. A high-resolution computed tomographic (CT) whole-animal post-mortem scan of one pig was also performed to verify the large sample CT capabilities of the IMBL. MCT tracking particles were visible in all animals, and the automated MCT tracking algorithms used were able to identify and track many particles, but accuracy was reduced when particles moved faster than $\sim$6 mm min^{-1} (50 pixels between exposures), or when the particles touched or overlapped. Renderings were successfully made from the CT data set. Technical issues prevented use of reliable shuttering and hence radiation doses were variable. Since dose must be carefully controlled in future studies, estimates of the minimum achievable radiation doses using this experiment design are shown. In summary, this study demonstrated the suitability of the IMBL for large-animal tracheal MCT imaging, and for whole-animal CT.

1. Introduction and objectives

In cystic fibrosis (CF), the defective CF transmembrane conductance regulator (CFTR) gene produces an ion imbalance in airway surface cells resulting in dehydration of the airway surface liquid (ASL). This change impairs the mucociliary transport (MCT) system, leading to an inability to clear mucus and inhaled particulates and pathogens from the lungs, progressive lung disease, and ultimately death from lung failure (Cutting, 2015). In other studies we have developed an airway gene-transfer method that uses a lentiviral vector to insert a functioning copy of the CFTR gene into CF-mouse-nasal-airway cells *in vivo*, with the resulting ion-channel
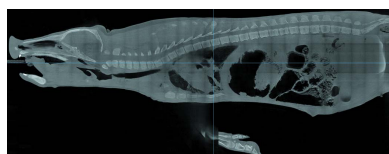
correction lasting for at least 12 months (Cmielewski *et al.*, 2014). Although we can measure airway-surface ionic changes produced by our gene therapy in live-CF-mouse nasal airways, by measuring the potential difference across the airway epithelium (Cmielewski *et al.*, 2014), the ability to accurately quantify MCT correction and improved airway health in live CF animals would be a major advance in the assessment of CF disease and treatments. However, CF mice are a poor model for therapeutics development in their lungs, since they do not exhibit human-like lung disease (Grubb & Boucher, 1999). β-ENaC mice (Zhou *et al.*, 2011), which show CF-like mucus-obstructive disease, are also unsuitable because they contain functioning CFTR ion channels, so lentiviral mediated CFTR gene expression is not therapeutically relevant.

One of the recently developed CF models currently available in the USA is the CF pig (Stoltz *et al.*, 2010). Within months of birth, CF pigs spontaneously develop characteristic features of CF lung disease including airway inflammation, remodelling, mucus accumulation, and infection. One way of assessing dysfunctional mucus clearance in live-animal models, particularly for diseases such as CF, is to examine how well the MCT system clears particles from the airway surface. Hoegger *et al.* (2014) therefore assessed MCT by tracking the motion of a small number of 350 µm-diameter × 25 µm-thickness tantalum micro discs placed in the airways of normal and CF pigs using a clinical-computed-tomography (CT) imaging system. After the particles were delivered to the airways a similar proportion of the discs were cleared from the airways in both the CF and normal lungs, and in both groups MCT drove the particles toward the ventral tracheal surface. Although treatment with the cholinergic agonist methacholine raised the ciliary beat frequency in both groups, it reduced the proportion of discs that cleared the CF lungs, suggesting that MCT responses are different in the two groups. Given that the absence of the CFTR gene produces CFTR protein defects in CF pig lungs that result in similar pathophysiology to humans, including impaired MCT, and that the size of their lungs are similar to human lungs, the pig is an ideal model in which to test the effectiveness of our gene-therapy treatment. The primary outcome measure is then assessment of the change in MCT velocity on the airway surface.

To determine the efficacy of new airway-rehydrating therapies designed to treat CF, our group has developed MCT monitoring methods that measure the transport velocity and behaviour (*e.g.* local-clearance direction and particle aggregation) of deposited MCT marker particles in a similar manner to that described by Hoegger *et al.* (2014). By using a propagation-based synchrotron phase-contrast X-ray imaging (PCXI) setup, we have imaged and quantified MCT in the nasal and lung airways of live anaesthetized normal, CFTR-null and β-ENaC mice (Donnelley, Morgan, Siu, Fouras *et al.*, 2014; Donnelley, Morgan, Siu, Farrow *et al.*, 2014). These X-ray imaging methods have been developed over the last decade at the SPring-8 synchrotron in Japan on the BL20XU beamline, where the high flux density allows fast imaging of very small regions of interest such as the ~1 mm-diameter mouse trachea.

PCXI has also been used by other groups for a range of respiratory imaging studies at different synchrotron facilities including the SPring-8 Synchrotron, Swiss Light Source, The European Synchrotron Radiation Facility, and the Canadian Light Source. PCXI setups are used primarily because the air–tissue interfaces enhance image contrast, enabling improved airway and lung visualization. Examples include image-based pulmonary function testing in β-ENaC mice (Stahr *et al.*, 2016), examination of how CF pig ASL responds to inhaled pathogens (Luan *et al.*, 2017), imaging the first breaths after birth (Hooper *et al.*, 2009), assessing regional aerosol deposition (Porra *et al.*, 2018), studying the inflation of alveoli at high magnification (Lovric *et al.*, 2017), and visualizing lung-tissue oscillations during lung-function testing (Thurgood *et al.*, 2016).

The Australian Synchrotron Imaging and Medical Beamline (IMBL) was primarily designed for performing propagation-based PCXI of large objects and for human clinical studies. It has a high coherence and intensity, as well as a large source-to-sample distance of ~137 m in the satellite building hutch, resulting in an X-ray beam of up to 400 mm × 40 mm (W × H) at the sample position, making the imaging of larger animals such as pigs possible. In recent pilot studies we used the IMBL to examine the MCT behaviour of deposited 100 µm high-refractive-index (HRI) glass-bead marker particles in freshly excised segments of sheep and pig trachea (Donnelley *et al.*, 2017). The clarity of the *ex vivo* data we obtained demonstrated the exciting potential of the IMBL for performing live-large-animal imaging once relevant large-CF-animal models, such as CF pigs, become available.

Our *ex vivo* imaging setup had obvious limitations; primarily the fact that the tissue was excised from the animal prior to imaging, and MCT behaviour is likely to be different in the absence of reciprocating airflow or careful control of air humidification. The current project was therefore designed to use PCXI to assess the transit of deposited marker particles in the trachea of live anaesthetized piglets. Our primary aim in this pilot study was to develop the appropriate animal handling, anaesthesia, restraint and imaging protocols for live-piglet imaging. Continuing from our *ex vivo* studies we validated the ability to track MCT in live-pig trachea using HRI glass-bead marker particles, and quantified the effect of standard pharmaceutical treatments known to alter MCT and compared this with our *ex vivo* data. Our secondary aim was to estimate the radiation dose delivered in this experiment, as well as the likely minimum achievable dose following protocol optimization, to enable future repeat-imaging experiments, including *in vivo* gene-therapy trials in CF pigs. Our final aim was to employ the large width of the beam at the IMBL to test the feasibility of large whole-animal CT.

2. Methods

2.1. Ethics statement

All experiments were performed on the Imaging and Medical Beamline at the Australian Synchrotron under

approvals from the animal ethics committees of the Australian Synchrotron (AS-2016-001), the University of Adelaide (M-2016-001) and the Women's and Children's Health Network (AE1028-03-2019).

2.2. Beamline setup

The beamline was configured in the same manner as described for our *ex vivo* sheep and pig-tracheal imaging experiments (Donnelley *et al.*, 2017), with some modifications. A sample-to-detector distance of ~4 m, an energy of 55 keV, and exposure times of 100 ms were used. These parameters were chosen to produce optimal soft-tissue contrast in these large animals, and to span the dynamic range (16-bits) of the PCO.edge sensor (PCO imaging, Germany). Images with an effective pixel size of 7.6 µm (field of view of ~19.5 mm × 16.5 mm) were captured using the Ruby detector (Hall *et al.*, 2013) to enable visualization of the full width of the pig trachea.

2.3. Animal preparation

Eight Large White/Landrace × Duroc piglets were studied. Seven animals were ~8 weeks old and ~20 kg, and one was ~6 weeks old and ~12.5 kg. Anaesthesia was induced with an intramuscular injection of a mix of atropine 30 µg kg^{-1}, ketamine 10 mg kg^{-1}, medetomidine 80 µg kg^{-1}, and butorphanol 200 µg kg^{-1}. Animals were intubated with a 7 Fr cuffed endotracheal tube (6 Fr for the small animal), with placement aided and confirmed with an Ambu aScope (Ballerup, Copenhagen). We aimed to insert the tube with a shallow placement, just distal to the epiglottis, to allow the tracheal airway surface to remain unperturbed.

Pigs were ventilated with 2% isoflurane (Advanced Anaesthesia Specialists) and 700 ml min^{-1} oxygen at a respiratory rate of ~15 br min^{-1}, an *I:E* ratio of 1:2, a positive inspiratory pressure of 15–20 cm H$_2$O, and a minute ventilation of 3.5 l, using a Datex Ohmeda 7000 ventilator. Once anaesthesia was stabilized the isoflurane concentration was reduced to 1% for imaging. Inspired air was warmed using a Darvall Heated Smooth-Wall circuit (Advanced Anaesthesia Specialists), but no humidification was used. Pigs were kept on

an intravenous Hartmann's solution drip to maintain hydration throughout the experiments. Heart rate, oxygen saturation, end tidal CO$_2$, and rectal temperature were all monitored throughout the experiment using a Cardell 9500 HD vital signs monitor, as well as a PowerLab (16/35, AD Instruments). An Aeroneb vibrating mesh nebuliser (Aerogen, Galway, Ireland) was placed into the inspiratory line of the ventilator circuit using a T-adaptor to deliver treatments.

For imaging, the pigs were placed supine on a patient table attached to a Kuka robotic arm integrated into the IMBL imaging hutch control system (Fig. 1a). The forelimbs were secured to ensure that they were not located in the imaging field of view. The animals were covered with a blanket throughout the experiment to maintain body temperature.

2.4. MCT marker particle delivery

A small sample of 200 µm-diameter HRI glass beads (Corpuscular, NY, USA), the same type used in our pilot *ex vivo* large-animal tracheal imaging experiments (Donnelley *et al.*, 2017), were loaded inside the distal end of a long delivery cannula (SurgiVet Bronco Alveolar Catheter, CBAL5190, Smiths Medical, MN, USA) by dipping the end into the bead sample and then cleaning the outside of the cannula. The loaded cannula was then fed into the endotracheal (ET) tube so that its tip was located ~10 mm past the end of the ET tube in the trachea. The other end of the delivery cannula was connected to a medical air supply *via* a pneumatic valve (Clippard EVO-3-12-L-M15, Cincinnati, OH, USA). When required, particles were delivered by opening the valve for 50 ms (electronically *via* the timing hub, see below).

2.5. MCT and lung imaging

In one animal, images of the tip of the delivery tube were captured at a higher frame rate (75 ms exposures; 13.3 frames s^{-1}) to record the particle-delivery process. In another animal, the peripheral lung tissue was examined at this higher frame rate to visualize the motion of the lung tissue and determine the visibility of the lung tissues. For the remainder of the MCT imaging study a timing hub with custom-designed hardware and control software was used to synchronize image capture. The Datex Ohmeda 7000 ventilator was modified to include a TTL output signal (high on inspiration), which was used as the synchronization input to the timing hub. After particle delivery, the hub was configured to acquire ten equispaced images throughout each breath for blocks of 12 breaths, acquired at the following time points: −2, −1, 0, 1, 2, 3, 4, 6, 9, 12, 15, 20, 25, and 30 min (the negative timepoints denote two baseline imaging periods prior to treatment delivery, with treatment delivery initiated at the start of the time 0 image block). The downstream shutter was set
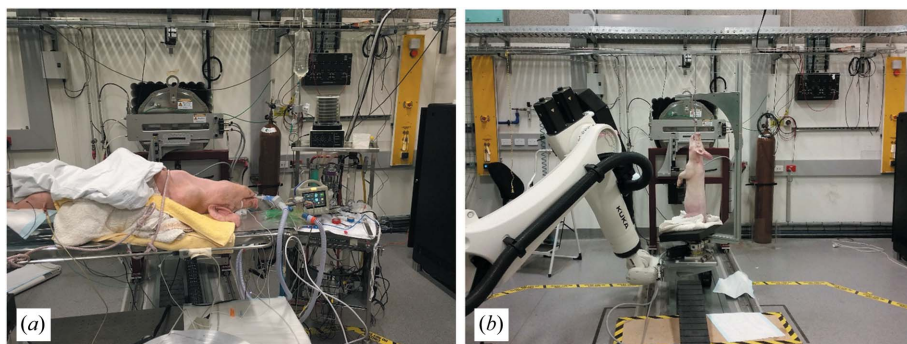

Figure 1
The IMBL imaging hutch setup for (a) MCT assessment in live-pig trachea with the ~20 kg pig lying supine on the patient table attached to the robotic arm, and (b) post-mortem CT of the ~12.5 kg pig using the custom-built large-animal holder secured to the rotation stage on the robotic arm.

to close between each block of images. This strategy was chosen to evaluate the time-course of changes in MCT in response to aerosols, while also reducing the radiation dose to the animals that would have otherwise resulted from continuous exposure to the X-ray beam.

Images of the pig trachea were captured from the lateral direction. At time point $t = 0$ the Aeroneb was used to deliver aerosolized isotonic saline to the airways and lungs. The Aeroneb was activated for 1.25 s on each inspiration for either 1.5 ($n = 3$) or 5 min ($n = 3$). At the completion of the imaging run the Aeroneb was cleaned and refilled with hypertonic saline. The same imaging sequence, aerosol delivery, and imaging process were then repeated with hypertonic saline.

At the completion of the experiments the pigs were humanely killed via Nembutal overdose without waking from anaesthesia.

The radiation dose was not directly measured in this experiment. Instead the dose was approximated based on measurements made in IMBL hutch 2B for a separate microbeam-radiation-therapy experiment (where accurate dose measurement is possible) that utilized the same beamline settings (energy and filtration, etc), taking into account the geometric scaling factor between the two imaging hutches. The dose is discussed further at the end of §3.1.

2.6. Post-experimental MCT analyses

Images were flat-field and dark-current corrected to minimize the effects of scratches or dust on the scintillator and inhomogeneities in the X-ray beam intensity, and speckle noise was reduced using an anisotropic diffusion filter (Lopes, 2014). Our previously described ex vivo image-analysis software (Matlab R2017a, The Mathworks, Natick, USA) was applied to measure and compare particle MCT rates and directionality by identifying particles and tracking their motion throughout the image sequences (Donnelley et al., 2017). For this in vivo study the software used a modified pre-processing stage: the background subtraction step used in our ex vivo studies was removed because it performed poorly with the constantly moving background that resulted from respiratory and cardiac movements. Instead, any images in which large respiratory motions caused blurring or a large translation of the airway were manually identified and removed from the sequences to improve the accuracy of the subsequent particle identification and tracking steps. Despite the flat-field correction the illumination remained uneven, so a discrete orthogonal polynomial toolbox from the University of Leoben (Harker & O'Leary, undated) was used to generate a two-dimensional polynomial approximation of the illumination field, and then correct the non-uniform illumination. The corrected image was used as the input to the circular Hough transform stage, meaning that no intensity thresholds were required for particle detection.

The large number of particles in each trachea meant that the number of possible tracking combinations that had to be evaluated was very large, so the previously utilized George-town University particle-tracking algorithm (Blair & Dufresne, 2005) was modified to increase the number of allowable steps before failure from 2×10^5 to 2×10^{10}. This change allowed the maximum particle displacement to be increased to 50 pixels. Particles that were tracked for less than four consecutive frames were excluded.

A manual analysis of the particle trajectories was also performed on the same sequences of images analysed by the automated algorithm, using the methods previously described (Donnelley, Morgan, Siu, Farrow et al., 2014). Briefly, a Matlab script was used to present blocks of images to an observer (MD), who manually tracked the locations of the moving particles throughout each of the image sequences (with the animal and time-point randomized and blinded).

Instantaneous tracking particle velocity histograms were generated as previously described (Donnelley et al., 2017), and supplementary movie files (.mp4 format, see supporting information) were assembled from the processed images to show the variability in particulate behaviour on the tracheal airway surfaces. The movie frame rate was set to ~20× normal speed. The videos can be played using the free VLC Media Player (available at http://www.videolan.org/vlc/). (Note that all video files are made avaliable on the IUCr YouTube channel when articles are published.)

2.7. Computed tomography

At the completion of MCT imaging the small six week old pig was humanely killed and then prepared for CT imaging. A rotation stage was placed on the robotic arm, and the pig was held head high using a custom-built frame (Fig. 1b). The detector was changed to a CMOS Flat Panel Sensor (C9252DK-14, Hamamatsu, Japan) with an effective pixel size of 10.6 μm × 10.6 μm, and a field of view of 27.1 mm × 22.9 mm (1216 × 616 pixels), and an exposure time of 40 ms was used. In all other respects the imaging setup remained the same. Because of the large sample size compared with the detector and X-ray beam, the axis of rotation was offset to the side of the field of view, and each CT scan was set to acquire 4000 projections over 360° (0.09° per image at an acquisition speed of 2.25° s^{-1}), along with a set of 30 flat-field and 30 dark-current images at the beginning of each scan. Between scans the robot arm was translated vertically to capture CT slices through the entire animal.

After imaging was completed the images were flat-field and dark-current corrected, the vertical scans stitched together into single projection images, and single-image phase retrieval (Paganin et al., 2002) was performed with a δ/β ratio of 200 as described by Murrie et al. (2015). The projection images were reconstructed into slices using X-TRACT software (Gureyev et al., 2011) on the Australian Synchrotron Compute Infrastructure (ASCI) computing cluster, using a filtered back-projection algorithm. Dynamic slices were obtained in Fiji (Schindelin et al., 2012), and volumes were rendered using Drishti (Limaye, 2012) and Amira-Avizo Fire 8.1 (Thermo-Fischer Scientific).

3. Results and discussion

3.1. MCT assessment

The imaging procedures were well tolerated by all animals. Because of technical challenges with the IMBL imaging setup, usable MCT tracking images were only available for one animal following isotonic saline aerosol delivery, but from six animals following hypertonic saline.

In each case, the MCT tracking particles were correctly delivered using the intra-tracheal delivery tube and solenoid-regulated air supply, with an appropriate number of particles present in the field of view. Fig. 2 shows two sequential frames taken 75 ms apart, before and after particle delivery. This delivery method proved to be repeatable, with a similar number and distribution of particles seen in each animal. Particle movement after delivery was heterogeneous, as we previously reported for our *ex vivo* study (Donnelley *et al.*, 2017). Most particles were stationary at the start of imaging, but some started moving when aerosolized hypertonic saline was applied. Beads tended to move towards the ventral tracheal surface (*i.e.* towards the top of the field of view), as well as being cleared towards the larynx, matching activity observed in our *ex vivo* pig-trachea experiments. An example of a raw image sequence prior to application of the particle-tracking algorithm is shown in Video S1 of the supporting information.

To quantify MCT, the motion of particles was tracked using the last image acquired in each breath (*i.e.* at end-expiration), because these frames were less subject to blurring from respiratory motion than the earlier frames in the breath. The automated particle-detection and tracking algorithm worked for all the image sequences except for one hypertonic saline treated animal in which there were too many fast-moving particles for the algorithm to track correctly. There were some false-negative and false-positive particle detections; when particles clumped closely together they were not detected as well as the isolated particles, and occasionally particle-like features within and outside the airway were detected. These false measurements were easily noted since the algorithm labels detected particles in the resulting movies. After the particles were detected in each image, tracking was performed to link their locations throughout the images in the sequence to form particle trajectories. In many sequences there were some fast-moving particles that were not automatically tracked correctly; a consequence of the 50 pixel tracking displacement limit that results in a maximum detectable MCT velocity of $\sim$6 mm min^{-1}. Increasing the maximum displacement resulted in failure of the tracking algorithm, because of the extremely large number of possible combinations that the tracking algorithm (Blair & Dufresne, 2005) would need to test. By comparison, the particles could be manually tracked in most images, although there were some sequences where even manual tracking was almost impossible, because of the inability to uniquely identify the particles across frames. The manual process was also very time-consuming because of the large number of particles that must be manually tracked throughout the image sequences ($\sim$36 h total analysis time), and therefore could not be applied to larger data sets. An example of automatically and manually tracked particles is shown in Fig. 3, and Videos S2 and S3, respectively (see supporting information).

The detection and tracking of the particles was substantially more difficult here than in our previous *ex vivo* experiment, because of the almost constant motion of the trachea that results from respiratory and cardiac motion. The small oscillating movement of the airway and beads between frames was challenging to isolate from real MCT motion since the magnitude and direction of the motion varied across the trachea and from breath to breath, and was dependent on which tracheal wall the particles are located (*i.e.* there are essentially two planes of motion to consider because the left and right lateral walls of the airway are superimposed under X-ray imaging). These factors meant that this motion could not be removed using a simple image-registration process, and its presence makes interpretation of the automated-tracking results more challenging. Development of more advanced particle-tracking techniques, as undertaken for the mouse nasal airway (Jung *et al.*, 2017), is required to allow complete measurement of particle MCT motion. In a number of the manually tracked data sets it was possible to perform quantitative MCT analysis as shown by the instantaneous velocity plot in Fig. 4. This shows that the particle transit speeds are of the magnitude expected in pig trachea, particles move predominantly in the expected direction, and that the delivery of aerosolized hypertonic saline produces a rapid and transient increase in MCT velocity.

A high-magnification fluoroscope-like image sequence was taken in one animal to visualize the motion of the
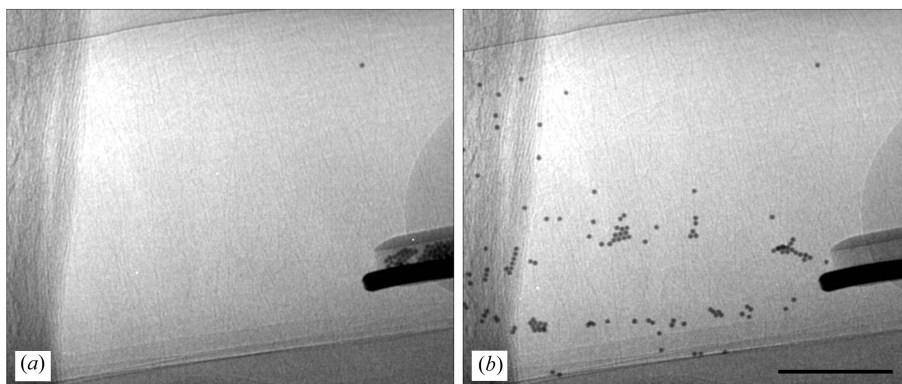

Figure 2
Two sequential frames of the pig trachea (*a*) immediately before and (*b*) after 200 μm HRI glass-bead MCT marker particle delivery. The tip of the ET tube is visible on the right side of the image, with the particle-delivery tube (and particles) visible inside it. The dense object is a wire that was placed inside the ET tube of the first animal to aid in locating the tip. No particle identification or tracking was performed on these two images, so particles are unmarked. Scale bar: 5 mm.
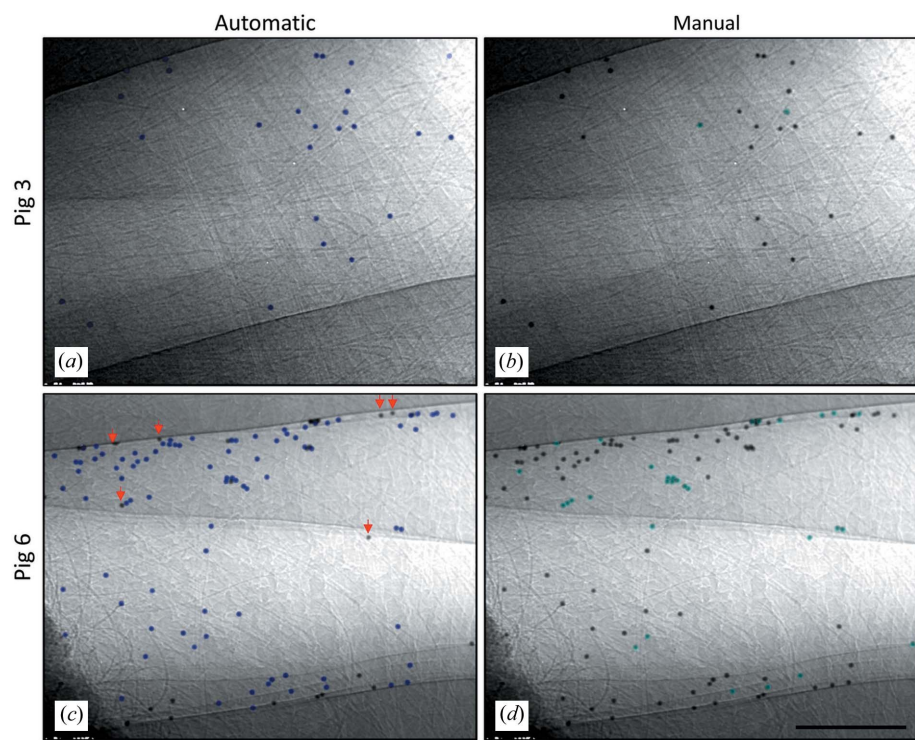
Martin Donnelley *et al.* · Live-pig-airway surface imaging and whole-pig CT

Figure 3
Example MCT particle-tracking results from pigs 3 and 6. Automatically tracked particles are shown in blue (left panels), and manually tracked particles are shown in green (right panels). Unmarked (*i.e.* not coloured) particles in the automatically tracked images were either not correctly detected or not tracked for a sufficient number of frames. Unmarked particles in the manually tracked images were not moving within that analysis time point. Red arrows in (*c*) indicate particles that were not correctly identified as moving by the automated tracking algorithm. Scale bar: 5 mm.

lungs and surrounding tissue. A short segment from this sequence is shown in Video S4 of the supporting information.

This first study revealed that our chosen image acquisition and ventilation strategies were not optimal for obtaining high-quality images, and several changes would enhance the quality and outcomes of future experiments. We expect that ventilating the pigs with dry oxygen can dehydrate the airway surface, reducing the MCT activity that we are trying to measure. Clearly this effect was not permanent because the addition of hypertonic saline aerosol caused MCT rates to transiently increase. However, for future studies we propose that it may be better to maintain the animals on the injectable anaesthetic for the duration of the study, to allow them to breathe freely without intubation and ventilation, thereby maintaining tracheal air humidity. Image acquisition in these large animals can be easily gated to respiration using a chest transducer (*e.g.* AD Instruments MLT1132) to detect changes in thor-
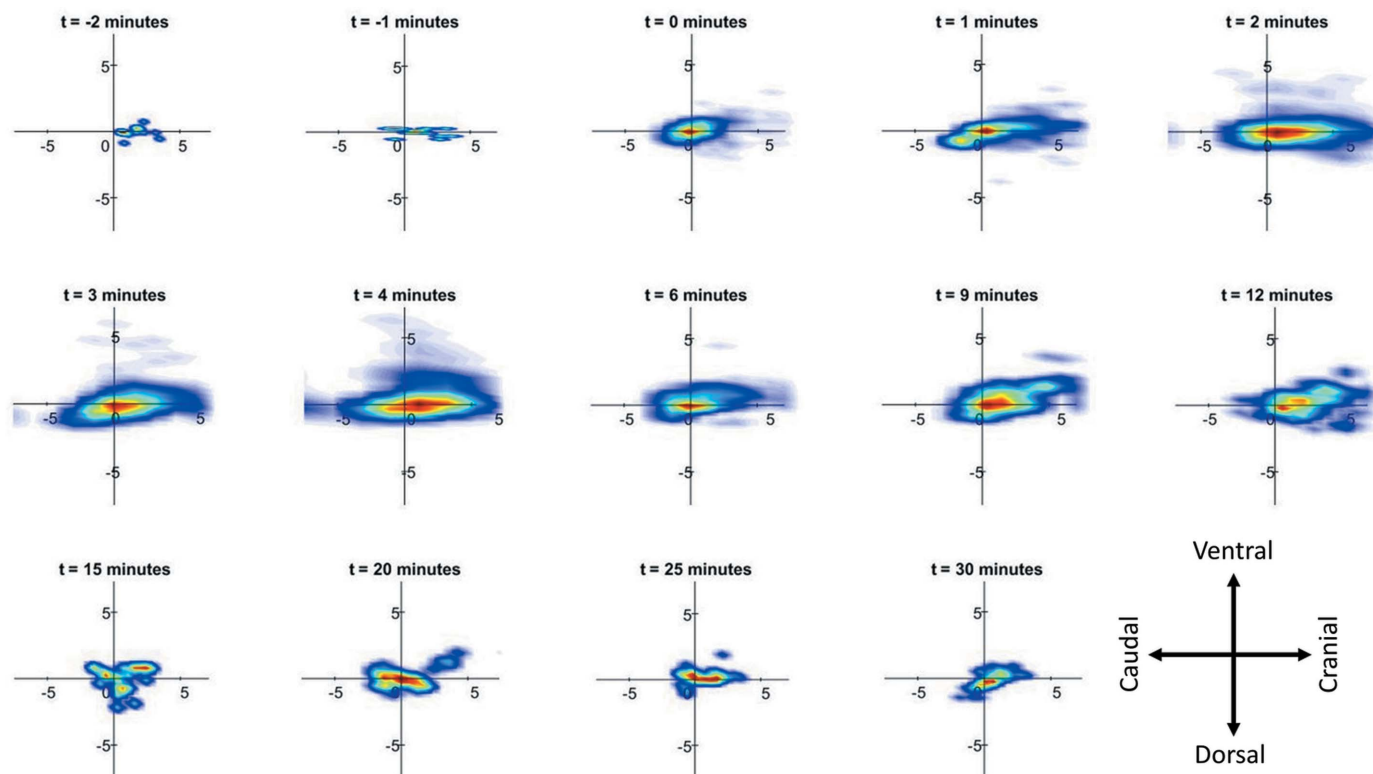

Figure 4
Motion histogram of the manual-tracking data from pig 6, showing changes in MCT velocity and direction over time following treatment with aerosolized hypertonic saline (beginning at $t = 0$). Clearance was predominantly in the cranial direction, towards the larynx (right). All axes in mm min^{-1}.

acic or abdominal circumference during breathing, with image capture still triggered by the timing hub. Despite using the timing hub and ventilator to control image acquisition, a small amount of motion blur of the particles was still present, indicating that the 100 ms exposure time was too long. For future studies, halving the exposure time would be beneficial, because improvements in the accuracy of particle detection from reduced blurring would likely outweigh the reduced signal-to-noise ratio from the shorter exposure length.

At the time that these experiments were performed, hardware triggering of the IMBL shutter was not available, so to reduce radiation dose we used a software script to open the shutter at the image acquisition times determined by our timing hub (this is normally an output signal from the timing hub). The IMBL control script was not reliable, and resulted in timing irregularities, including blocks of images being missed in some animals, and the shutter remaining open for too long in others. Because of the script design, image acquisition also began at a random point in the breath, creating additional analysis challenges that were solved by manually examining the *LabChart* data recording to note where in the breath acquisition started. For some animals, images were missing because the camera did not acquire correctly.

The dose-rate measured in the upstream IMBL hutch 2B was 6.75 Gy s^{-1}. Taking into account the geometric factor moving from 2B at 32.8 m to 3B at 135.8 m from the source gives a dose rate of 0.39 Gy s^{-1}. As a result of the timing and shuttering challenges, as well as the acquisition of the high-frame-rate movies, the delivered radiation doses delivered in these studies were variable. Since we also made no effort to reduce the dose for this experiment, rather than reporting the delivered dose we have estimated the minimum dose that could now be achieved with correct shuttering and optimized

image acquisition timing. Our imaging protocol acquired 14 × 1 minute blocks of images over a ~32 minute period, with ~12 images per block (168 images total). Calculating MCT behaviour requires acquisition of one 100 ms exposure per breath, so, with correct shuttering, we expect a total exposure time of 16.8 s, or a dose of 6.5 Gy delivered to the tracheal imaging region. Shortening the exposure length to 50 ms, combined with further improvements in detector technology (such as more efficient scintillators and more sensitive sCMOS chips) that might allow for further decreases, would together dramatically reduce the delivered radiation dose to more physiologically acceptable levels.

3.2. CT imaging

The aim of this part of the experiment was to verify that the IMBL could be used to produce high-quality post-mortem CT images of a large animal. Since this was the first time such a large biological sample was imaged at the IMBL there were setup delays of ~5.5 h between when the animal was humanely killed at the end of the MCT imaging and the CT scan starting, in order to set up the custom-built large-animal holder and rotation stage on the robotic arm. Imaging of the whole pig was completed in 29 separate vertically translated scans (total scan time 3.5 h) that were stitched together in post-processing. This resulted in a total of 3748 reconstructed slices to capture the head to the tail of the pig. Example orthogonal reconstructions through the lung are shown in Fig. 5, a rendering of the whole animal is shown in Fig. 6, and a slice through the pig nasal airway is shown in Fig. 7. These renderings demonstrate the ability to image an animal around 1 m in length, while maintaining the spatial resolution necessary to detect sub-millimetre features like the nasal airways.

Figure 5
Example-orthogonal-reconstructed slices through the entire pig carcass. The slices are presented to show detail in the lung.

Figure 6
Example rendering of the pig carcass, designed to highlight the respiratory and skeletal systems.
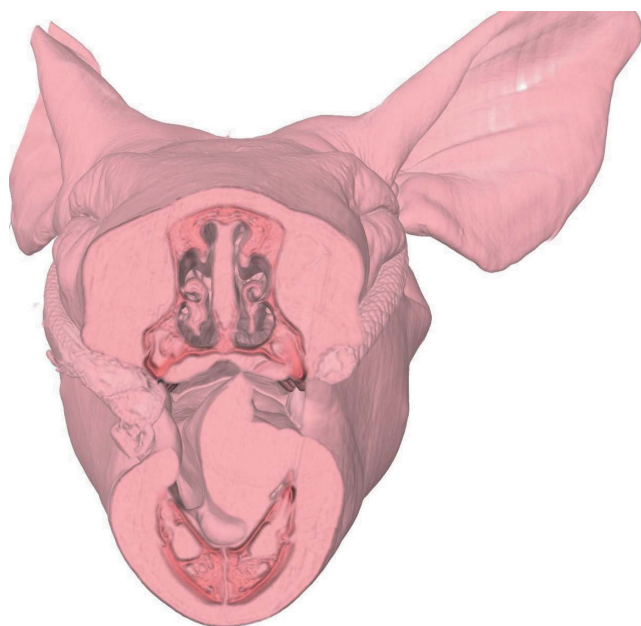

Figure 7
Example rendering of the pig nasal airway, showing the capabilities of the IMBL large-animal CT system for airway phase-contrast imaging.

4. Conclusion

During this experiment we tested animal handling, anaesthesia, restraint and imaging protocols for live-piglet imaging at the IMBL. We demonstrated the feasibility of performing tracheal MCT assessments in live-pig trachea, with animal handling and the delivery of sub-millimetre particles to the airways well controlled. Although our chosen anaesthesia, ventilation and imaging strategy did not produce perfect imaging results, we identified the key factors for improvement. In future studies, higher-quality-airway MCT assessments can be gained by allowing the animals to breathe freely with respiration detected using a respiratory band; by using shorter exposure lengths; and by using an improved shuttering system. The ability to perform capture whole-pig CT imaging with the assistance of a positioning robot has also been demonstrated.

References

Blair, D. & Dufresne, E. (2005). *The Matlab Particle Tracking Code Repository*, http://site.physics.georgetown.edu/matlab/.

Cmielewski, P., Donnelley, M. & Parsons, D. W. (2014). *J. Gene Med.* **16**, 291–299.

Cutting, G. R. (2015). *Nat. Rev. Genet.* **16**, 45–56.

Donnelley, M., Morgan, K. S., Awadalla, M., Farrow, N. R., Hall, C. & Parsons, D. W. (2017). *Respir. Res.* **18**, 95

Donnelley, M., Morgan, K. S., Siu, K. K., Farrow, N. R., Stahr, C. S., Boucher, R. C., Fouras, A. & Parsons, D. W. (2014). *Sci. Rep.* **4**, 3689.

Donnelley, M., Morgan, K. S., Siu, K. K., Fouras, A., Farrow, N. R., Carnibella, R. P. & Parsons, D. W. (2014). *J. Synchrotron Rad.* **21**, 768–773.

Grubb, B. R. & Boucher, R. C. (1999). *Physiol. Rev.* **79**, S193–S214.

Gureyev, T. E., Nesterets, Ya., Ternovski, D., Thompson, D., Wilkins, S. W., Stevenson, A. W., Sakellariou, A. & Taylor, J. A. (2011). *Proc. SPIE*, **8141**, 81410B.

Hall, C., Hausermann, D., Maksimenko, A., Astolfo, A., Siu, K., Pearson, J. & Stevenson, A. (2013). *J. Instrum.* **8**, C06011.

Harker, M. & O'Leary, P. (undated). *Diecrete Orthogonal Polynomials: Dopbox Version V1.8*, http://au.mathworks.com/matlabcentral/fileexchange/41250-discrete-orthogonal-polynomial-toolbox-dopbox-version-1-8.

Hoegger, M. J., Fischer, A. J., McMenimen, J. D., Ostedgaard, L. S., Tucker, A. J., Awadalla, M. A., Moninger, T. O., Michalski, A. S., Hoffman, E. A., Zabner, J., Stoltz, D. A. & Welsh, M. J. (2014). *Science*, **345**, 818–822.

Hooper, S. B., Kitchen, M. J., Siew, M. L. L., Lewis, R. A., Fouras, A. B., te Pas, A., Siu, K. K. W., Yagi, N., Uesugi, K. & Wallace, M. J. (2009). *Clin. Exp. Pharmacol. Physiol.* **36**, 117–125.

Jung, H.-W., Lee, S.-H., Donnelley, M., Parsons, D. & Lee, I. (2017). *Expert Syst. Appl.* **73**, 57–68.

Limaye, A. (2012). *Proc. SPIE*, **8506**, 85060X.

Lopes, D. (2014). *Anisotrophic Diffusion (Perona & Malik)*, https://au.mathworks.com/matlabcentral/fileexchange/14995-anisotropic-diffusion-perona-malik.

Lovric, G., Mokso, R., Arcadu, F., Vogiatzis Oikonomidis, I., Schittny, J. C., Roth-Kleiner, M. & Stampanoni, M. (2017). *Sci. Rep.* **7**, 12545.

Luan, X., Belev, G., Tam, J. S., Jagadeeshan, S., Hassan, N., Gioino, P., Grishchenko, N., Huang, Y., Carmalt, J. L., Duke, T., Jones, T., Monson, B., Burmester, M., Simovich, T., Yilmaz, O., Campanucci, V. A., Machen, T. E., Chapman, L. D. & Ianowski, J. P. (2017). *Nat. Commun.* **8**, 786.

Murrie, R. P., Morgan, K. S., Maksimenko, A., Fouras, A., Paganin, D. M., Hall, C., Siu, K. K. W., Parsons, D. W. & Donnelley, M. (2015). *J. Synchrotron Rad.* **22**, 1049–1055.

Paganin, D., Mayo, S. C., Gureyev, T. E., Miller, P. R. & Wilkins, S. W. (2002). *J. Microsc.* **206**, 33–40.

Porra, L., Dégrugilliers, L., Broche, L., Albu, G., Strengell, S., Suhonen, H., Fodor, G. H., Peták, F., Suortti, P., Habre, W., Sovijärvi, A. R. A. & Bayat, S. (2018). *Sci. Rep.* **8**, 3519.

Schindelin, J., Arganda-Carreras, I., Frise, E., Kaynig, V., Longair, M., Pietzsch, T., Preibisch, S., Rueden, C., Saalfeld, S., Schmid, B., Tinevez, J. Y., White, D. J., Hartenstein, V., Eliceiri, K., Tomancak, P. & Cardona, A. (2012). *Nat. Methods*, **9**, 676–682.

Stahr, C. S., Samarage, C. R., Donnelley, M., Farrow, N., Morgan, K. S., Zosky, G., Boucher, R. C., Siu, K. K. W., Mall, M. A., Parsons, D. W., Dubsky, S. & Fouras, A. (2016). *Sci. Rep.* **6**, 29438.

Stoltz, D. A., Meyerholz, D. K., Pezzulo, A. A., Ramachandran, S., Rogan, M. P., Davis, G. J., Hanfland, R. A., Wohlford-Lenane, C., Dohrn, C. L., Bartlett, J. A., Nelson, G. A., Chang, E. H., Taft, P. J., Ludwig, P. S., Estin, M., Hornick, E. E., Launspach, J. L., Samuel, M., Rokhlina, T., Karp, P. H., Ostedgaard, L. S., Uc, A., Starner, T. D., Horswill, A. R., Brogden, K. A., Prather, R. S., Richter, S. S., Shilyansky, J., McCray, P. B., Zabner, J. & Welsh, M. J. (2010). *Sci. Transl. Med.* **2**, 29–31.

Thurgood, J., Dubsky, S., Uesugi, K., Curtis, M., Samarage, C. R., Thompson, B., Zosky, G. & Fouras, A. (2016). *J. Synchrotron Rad.* **23**, 324–330.

Zhou, Z., Duerr, J., Johannesson, B., Schubert, S. C., Treis, D., Harm, M., Graeber, S. Y., Dalpke, A., Schultz, C. & Mall, M. A. (2011). *J. Cystic Fibrosis*, **10**, S172–S182.